General guidelines for the performance of viscoelastic property identification in elastography: A Monte-Carlo analysis from a closed-form solution

Elijah van Houten, Giuseppe Geymonat, Françoise Krasucki, Bertrand Wattrisse

Received: 9 September 2022 | Revised: 6 May 2023 | Accepted: 21 May 2023

DOI: 10.1002/cnm.3741

BASIC RESEARCH

WILEY

General guidelines for the performance of viscoelastic property identification in elastography: A Monte-Carlo analysis from a closed-form solution

Elijah Van Houten[1] | **Giuseppe Geymonat**[2] | **Françoise Krasucki**[3] | **Bertrand Wattrisse**[4]

[1]Département de génie mécanique, Université de Sherbrooke, Québec, Canada

[2]Laboratoire de Mécanique des Solides, Institut Polytechnique de Paris, Paris, France

[3]IMAG, Université de Montpellier, Montpellier, France

[4]LMGC, Université de Montpellier, Montpellier, France

Correspondence
Elijah Van Houten, Département de génie mécanique, Université de Sherbrooke, 2500, boul. de l'Université, Sherbrooke, Québec, Canada J1K 2R1.
Email: eew.vanhouten@usherbrooke.ca

Abstract

Identification of the mechanical properties of a viscoelastic material depends on characteristics of the observed motion field within the object in question. For certain physical and experimental configurations and certain resolutions and variance within the measurement data, the viscoelastic properties of an object may become non-identifiable. Elastographic imaging methods seek to provide maps of these viscoelastic properties based on displacement data measured by traditional imaging techniques, such as *magnetic resonance* and *ultrasound*. Here, 1D analytic solutions of the viscoelastic wave equation are used to generate displacement fields over wave conditions representative of diverse time-harmonic elastography applications. These solutions are tested through the minimization of a least squares objective function suitable for framing the elastography inverse calculation. Analysis shows that the damping ratio and the ratio of the viscoelastic wavelength to the size of the domain play critical roles in the form of this least squares objective function. In addition, it can be shown analytically that this objective function will contain local minima, which hinder discovery of the global minima via gradient descent methods.

KEYWORDS

closed-form viscoelasticity, elastography, Monte-Carlo, viscoelastic waves

1 | INTRODUCTION

Image-based elastography has become a widely used and researched adjunct to traditional medical imaging techniques. From a clinical point of view, elastography aims to provide quantitative methods to replace traditional, subjective, auscultation and palpation exams in which the physician imposes a mechanical solicitation to the patient's body and interprets the felt response in terms of stiffness. From a practical point of view, the use of imaging data allows for the characterization of heterogeneous maps of mechanical properties, which is particularly suited for investigating complex biological and living systems with intricate mechanical structures including distributed and focal lesions such as fibrosis, inflammation or cancerous tumors.

Different imaging sources, based on different physical phenomena (ultrasound imaging,[1] optical coherence tomography,[2] magnetic resonance imaging,[3,4] etc.) can be used to obtain the displacement fields utilized for mechanical characterization of the system. *Elastography techniques postulate a type of mechanical behavior for the tissue* (in general: linear elasticity,[5] viscoelasticity[6,7] or poroelasticity[8–10]) and introduce a functional dependence on the parameters associated with the chosen material model to develop the best fit to the measured displacement data. The exact form of this functional relationship, and the methodology used to obtain the best agreement with the measurement data can vary widely between different elastography methods.[11–14]

In general, the acquisition chain associated with elastography is very complex as it involves the interaction of a variety of different physical phenomena, such as electromagnetic or acoustic fields interacting with mechanical vibrations. Furthermore, elastographic image reconstruction involves the resolution of a generally poorly conditioned inverse problem involving vector wave propagation in a heterogeneous, deformable media submitted to complex mechanical loading.[15–17] The demand from clinicians tends toward ever higher spatial resolutions to allow more detailed and precise clinical analysis. In this context, the metrological characterization of the elastographic imaging process as a whole is very complicated.[18,19] Here, we focus only on the mechanical aspect of the problem to establish a basic understanding of this critical step of the process, which can be coupled with the analysis of other steps in the imaging pipeline to develop an overall vision of the capacity and limitations of elastography imaging in different clinical and mechanical contexts.

The goal of this article is to establish the key parameters and limits influencing the elastographic characterization of the mechanical properties of a viscoelastic material in typical elastography conditions. In conventional elastography applications, the ensemble of imaging parameters are fixed, for example, measurement noise, image resolution, actuation amplitude and frequency, etc. The goal here is to highlight, in a simplistic situation, the main parameters governing the reconstruction sensitivity and stability with respect to the underlying viscoelastic properties of the material (i.e., tissue) being imaged. The long term goal is to use this information to help guide the clinical application of elastography methods, either by enhancing the technical development of these reconstruction methods to obtain the optimal results in a variety of imaging cases or by providing clinical users with indicators and strategies to guide imaging protocol development.

In this article, we study a simple uni-dimensional continuum formulation corresponding to a homogeneous rod submitted to a time-harmonic either traction-compression or shear wave (they are equivalent in 1D). This situation is representative of the *local scale* at which material property identification is performed.[20] The use of a 1D model for this study is justified by the fact that, for small deformations in 3D situations, the wave patterns correspond to the superposition of multiple 1D waves. In addition, in numerous elastograhy applications, compressional waves are either suppressed by the curl operator, or simply neglected via an incompressibile formulation, so that only one wave component is considered for mechanical property identification. Finally, numerous elastography methods rely on the identification of the propagating wavelength along a specified direction, via directional filtering, and are thus equivalent to a 1D approach.

Here we propose identification via a least-squares identification functional, built on the difference between measured and modeled displacements,[21] which generalizes the widely used condition for displacement-based elastography imaging. The use of an analytic solution of the continuum problem allows for quick computation of this functional and also for some analytical developments illustrating some of its intrinsic characteristics. Naturally, the biases on the displacement field depend on the imaging technique.[22] Here, we have chosen to represent these biases by their statistical distribution, and we have used a centered Gaussian distribution with different standard deviations. Using this simplistic *elastography model*, we investigate the influence of several experimental parameters (e.g., time-harmonic frequency, geometry, material properties, noise) on the quality of the identified mechanical properties. The proposed approach can be extended to other identification strategies (direct inversion,[23,24,5] virtual fields,[25] constitutive equation gap,[13] etc.).

Until now, there has been very little investigation of the fundamental limits of elastography methods. Barbone et al.[15] and McGarry et al.[16] have investigated the uniqueness of the elastographic inverse problem in certain conditions. The propagation of noise through different elastography reconstruction methods is often presented in work describing the methods themselves.[26–28] However, these investigations are limited to a specific imaging case, and often only a few different noise cases, and do not explore the range of imaging parameters investigated here, for example, measurement noise, image resolution, actuation amplitude and frequency, etc., nor do they present these studies in the context of a Monte-Carlo type study investigating the behavior across a large number of purturbations.

2 | METHODS

2.1 | A 1D analytic solution for the homogeneous viscoelastic wave equation

We consider the homogeneous 1D situation corresponding to a uniaxial, viscoelastic rod of length L and complex valued stiffness C and mass density ρ, submitted to harmonic solicitation at the pulsation frequency ω. Here, we consider the case of Dirichlet boundary conditions at one end, $x=0$, and generalized, non-homogeneous, boundary conditions at the opposing end, $x=L$. This leads to the following boundary value problem:

$$\begin{cases} \dfrac{d\sigma}{dx}+\rho\omega^2 u=0 \quad \text{for} \quad 0<x<L, \\ \sigma=C\dfrac{du}{dx}, \\ u(0)=\phi(0) \quad \text{and} \quad h\dfrac{du}{dx}(L)+ku(L)=\phi(L). \end{cases} \tag{1}$$

Here, $u(x)$ and $\sigma(x)$ are the 1D displacement field and the stress distribution in the rod, respectively, while the couple (h,k) represents the type of the applied boundary conditions at the end $x=L$ while $\phi(L)$ is the value of the imposed boundary conditions at this end. In our case, we will assume:

$$C=A+jB, \quad A>0, \quad B\geq 0, \tag{2}$$

where A and B represent the storage and loss modulus of the viscoelastic material, respectively. Here we propose a simple case of linear viscoelasticity, where the storage and loss modulus have no fixed relationship. The proposed approach could be naturally extended to more generalized models which consider the frequency dependence of these moduli, such as the fractional model presented by Wang et al.,[29] incorporating the relaxation time spectrum of the material which is not considered for characterization here. The solution of the equation is given by:

$$u(x)=a\exp(sx)+b\exp(-sx), \tag{3}$$

where a and b are two constants depending on the applied boundary conditions, and

$$C=|C|\exp(j\varphi) \quad 0\leq\varphi<\pi/2, \tag{4}$$

with phase angle φ such that

$$\cos(\varphi)=\frac{A}{|C|} \quad \sin(\varphi)=\frac{B}{|C|}$$

leading to

$$s=\omega\sqrt{\frac{\rho}{|C|}}\left\{\sin\left(\frac{\varphi}{2}\right)-j\cos\left(\frac{\varphi}{2}\right)\right\},$$

or, equivalently:

$$s=\frac{\omega}{|C|}\sqrt{\frac{\rho}{2}}\left\{\sqrt{|C|-A}-j\sqrt{|C|+A}\right\}. \tag{5}$$

Hence:

$$\Re(s)=\frac{\omega}{|C|}\sqrt{\frac{\rho}{2}}\sqrt{|C|-A} \quad \text{and} \quad \Im(s)=-\frac{\omega}{|C|}\sqrt{\frac{\rho}{2}}\sqrt{|C|+A}. \tag{6}$$

In this case, the viscoelastic parameters of shear stiffness, μ, and damping ratio, ξ, are expressed as:

$$\mu = \frac{2|C|^2}{|C| + A} > 0 \tag{7}$$

and

$$\xi = \frac{B}{2A} \geq 0, \tag{8}$$

respectively.

Let us remark that the correspondence between (A, B) and (μ, ξ) is an indefinitely differentiable bijection. Hence,

$$|C| = \frac{\mu}{2}\left(1 + \frac{1}{\sqrt{1+4\xi^2}}\right)$$

and

$$\mathfrak{R}(s) = \omega\sqrt{\frac{\rho}{\mu}}\left(\frac{2\xi}{1+\sqrt{1+4\xi^2}}\right) \quad \text{and} \quad \mathfrak{I}(s) = -\omega\sqrt{\frac{\rho}{\mu}}. \tag{9}$$

The wavelength of the viscoelastic shear wave, λ, is then given by

$$\lambda = \frac{2\pi}{\omega}\sqrt{\frac{\mu}{\rho}} = 2\pi|\mathfrak{I}(s)|^{-1}. \tag{10}$$

For later use we remark that with the previous notations

$$s = \frac{2\pi}{\lambda}\left(\frac{2\xi}{1+\sqrt{1+4\xi^2}} - j\right) = \omega\sqrt{\frac{\rho}{\mu}}\left(\frac{2\xi}{1+\sqrt{1+4\xi^2}} - j\right) \tag{11}$$

and

$$\mathfrak{I}(s) = -\frac{2\pi}{\lambda} \text{ and } \mathfrak{R}(s) = -\mathfrak{I}(s)\left(\frac{2\xi}{1+\sqrt{1+4\xi^2}}\right). \tag{12}$$

In order that the solution u defined by (3) be completely determined, one has to establish constants a and b that are consistent with the specified boundary conditions. This condition leads to the linear system

$$\begin{cases} a + b = \phi(0) \\ a(hs+k)\exp(sL) + b(-hs+k)\exp(-sL) = \phi(L). \end{cases} \tag{13}$$

whose determinant is

$$D = 2h\cosh(sL) + 2k\sinh(sL). \tag{14}$$

When $D \neq 0$, the system (13) has a unique solution and hence u can be explicitly defined on the domain $0 < x < L$. For the current application, we define a simple, non-trivial case where $u(0) = \phi(0) = 0$. Typically, in elastography applications, it is the displacement field that is measured and, if needed, used as boundary conditions, corresponding to the case $h = 0$ and $k = 1$, such that $u(L) = \phi(L) = u_L$. In this case, if $D \neq 0$, we have

$$u(x) = \frac{u_L}{\exp(sL) - \exp(-sL)}(\exp(sx) - \exp(-sx)) = \frac{u_L}{\sinh(sL)}\sinh(sx). \tag{15}$$

Recalling that $\sinh(\alpha + j\beta) = \sinh(\alpha)\cos(\beta) + j\cosh(\alpha)\sin(\beta)$, the condition $D \neq 0$ means that $|\sinh(sL)|^2 = \sinh^2(\Re(s)L) + \sin^2(\Im(s)L) \neq 0$. From (12) $\sinh^2(\Re(s)L) + \sin^2(\Im(s)L) = 0$ if and only if

$$\xi = 0 \text{ and } \lambda = \frac{2L}{m} \tag{16}$$

for some integer $m > 0$, which corresponds to the *resonance conditions* ($\lambda = \frac{2L}{m}$) for a *perfectly elastic material* ($\xi = 0$). Therefore the condition $D \neq 0$ is in general satisfied.

As it can be seen in Equation (11), s can be expressed as uniquely a function of mechanical properties (μ, ξ, ρ) and the pulsation, ω. Consequently, the solution $u(x)$ can be expressed in terms of the *material viscoelastic properties* of shear stiffness and damping ratio, (μ, ξ), and the mass density, ρ. We define the set of *mechanical properties*, $\theta := (\mu, \xi, \rho) \in \mathcal{M} := \{(\mu, \xi, \rho); \mu, \rho > 0, \xi \geq 0\}$, and the set of *test parameters* for a given choice of boundary conditions corresponding to a specified value of the couple (h, k), $Z := (L, \omega, \phi(L) = u_L) \in \mathcal{T} := \{(L, \omega, u_L); \omega, L > 0\}$, which define the geometry, the pulsation and the boundary conditions. In the case studied here, where Dirichlet boundary conditions are specified, such that $(h = 0, k = 1)$, the loading conditions simplify to $\phi(L) = u_L$.

Let us also remark that when $\omega = 0$, $u(x) = u_L \frac{x}{L}$ and hence the dependence on the material parameters disappears in this case. More precisely, we have the following asymptotic development in terms of powers of ωL:

$$u(x) = u_L \frac{x}{L}\left\{1 + \omega^2 L^2 \left(\frac{x^2}{L^2} - 1\right)\mathcal{A} + \cdots\right\}, \tag{17}$$

where $\mathcal{A}$ can be explicitly computed in terms of the material parameters. Thus at low frequencies, that is, $\frac{\lambda}{L} \gg 1$, the impact of the material parameters is determined by the value of $\omega^2 L^2 \mathcal{A}$ compared to 1.

2.2 | Least-square identification

The aim of the identification procedure is to estimate the material's mechanical properties $\theta_* = (\mu_*, \xi_*, \rho_*) \in \mathcal{M}$ based on displacement measurements, $u_m(x)$, in a suitable testing situation, $Z_* := (L_*, \omega_*, u_{*L_*})$. Here, we consider the mass density, pulsation frequency and geometry to be known a priori, that is, $\rho = \rho_*$, $L = L_*$, and $\omega = \omega_*$, while the boundary conditions are known imperfectly, so that u_L can be different from u_{*L}. In this case, the set of mechanical properties to be identified is reduced to the viscoelastic properties $\theta = (\mu, \xi)$. This will be achieved with the following least square procedure, *given the testing situation* $Z \in \mathcal{T}$. Let $u(\theta; Z)$ be the solution of Equation (1) for a given choice of the coefficients $\theta \in \mathcal{M}$ and let the *least square identification functional* $F(\theta; Z)$ be

$$F(\theta; Z) := \frac{1}{2}\int_0^L |u(\theta; Z)(x) - u_m(x)|^2 dx. \tag{18}$$

Then, the identification procedure is

$$\text{Minimize } F(\theta; Z) \text{ for } \theta \in \mathcal{M} \tag{19}$$

and

$$\theta^\diamond = (\mu^\diamond, \xi^\diamond) \in \arg\min F(\theta; Z) \tag{20}$$

is called *the most likely estimate of the viscoelastic properties for the test situation* $Z \in \mathcal{T}$. Developing $F(\theta;Z)$, one gets

$$F(\theta;Z) = \frac{1}{2}\int_0^L |u(\theta;Z)(x)|^2 dx + \frac{1}{2}\int_0^L |u_m(x)|^2 dx$$

$$- \int_0^L \Re\left[u(\theta;Z)(x)\overline{u_m(x)}\right] dx. \tag{21}$$

Let us remark that

$$\int_0^L |u(\theta;Z)(x)|^2 dx =$$

$$= \frac{|u_L|^2}{\sinh^2(\Re(s)L) + \sin^2(\Im(s)L)} \int_0^L \left[\sinh^2(\Re(s)x) + \sin^2(\Im(s)x)\right] dx =$$

$$= \frac{|u_L|^2}{\sinh^2(\Re(s)L) + \sin^2(\Im(s)L)} \left[\frac{\sinh(2\Re(s)L)}{4\Re(s)} - \frac{\sin(2\Im(s)L)}{4\Im(s)}\right]. \tag{22}$$

Let us also explicitly point out that $\left[\frac{\sinh(2\Re(s)L)}{4\Re(s)} - \frac{\sin(2\Im(s)L)}{4\Im(s)}\right] > 0$ when $L > 0$.

2.2.1 | A particular case: no model error and no noise

In the sequel, we consider the situation where the measured displacement is consistent with the above-mentioned viscoelastic model, so that one can write $u_m(x) = u(\theta_m;Z_m)(x)$ for a given choice of $\theta_m = (\mu_m, \xi_m) \in \mathcal{M}$ in the test situation $Z_m = (\omega_m, L_m, u_{mL_m}) \in \mathcal{T}$. Furthermore, if the test configuration is supposed to be perfectly known, that is, $Z = Z_m$, it is possible to completely compute $F(\theta;Z)$ since (21) gives

$$F(\theta;Z) = \left\{\frac{1}{2}\frac{1}{\sinh^2(\Re(s)L) + \sin^2(\Im(s)L)}\left[\frac{\sinh(2\Re(s)L)}{4\Re(s)} - \frac{\sin(2\Im(s)L)}{4\Im(s)}\right] + \right.$$

$$+ \frac{1}{2}\frac{1}{\sinh^2(\Re(s_m)L) + \sin^2(\Im(s_m)L)}\left[\frac{\sinh(2\Re(s_m)L)}{4\Re(s_m)} - \frac{\sin(2\Im(s_m)L)}{4\Im(s_m)}\right] -$$

$$\left. - \Re\left[\frac{1}{\sinh(sL)}\frac{1}{\sinh(\overline{s_m}L)}\int_0^L [\sinh(sx)\sinh(\overline{s_m}x)]dx\right]\right\} |u_L|^2. \tag{23}$$

Note that this expression defines the cost function $F(\theta;Z)$ in the particular situation where there is *no model error* (on the material behavior and on the boundary conditions) and no noise on the measured data. In this case, the last integral can be easily computed since

$$2\sinh(sx)\sinh(\overline{s_m}x) = \cosh((s+\overline{s_m})x) - \cosh((s-\overline{s_m})x)$$

obtaining:

$$\int_0^L [\sinh(sx)\sinh(\overline{s_m}x)]dx = \frac{\sinh((s+\overline{s_m})L)}{2(s+\overline{s_m})} - \frac{\sinh((s-\overline{s_m})L)}{2(s-\overline{s_m})}. \tag{24}$$

Since we have the complete expression of $F(\theta;Z)$, we can at least formally compute its derivatives with respect to s and also with respect to θ. A first examination of (23) immediately gives that $\min F(\theta;Z) = F\left(\theta^{\diamond};Z\right) = 0$ if and only if

$$\frac{\sinh(sx)}{\sinh(sL)} = \frac{\sinh(s_m x)}{\sinh(s_m L)} \quad \text{for all } 0 < x < L. \tag{25}$$

This equation is satisfied if $\theta^{\diamond} = \theta_m$. However, since the function $\frac{\sinh(sx)}{\sinh(sL)} - \frac{\sinh(s_m x)}{\sinh(s_m L)}$ is not convex with respect to s and *a fortiori* with respect to (θ,ρ) we see that the function $F(\theta;Z)$ can have many local minima making efficient numerical identification of the material properties a challenging task, even in this ideal situation.

2.3 | Objective function analysis of the solution space

The test conditions involve three types of parameters representing respectively: (*i*) the mechanical loading pulsation frequency (via parameter ω), (*ii*) the domain geometry (parameter L) and (*iii*) the applied boundary conditions (parameter u_L). In most elastography applications, the pulsation is very finely tuned and the geometry of the system is known. The most uncertain test condition is generally related to the boundary conditions. In the following, we will consider that the boundary condition u_L used to establish the displacement field, $u(x)$, corresponds to that used for the generation of the measured displacement field, $u_m(x)$, corrupted by a quantity δu_L, so that

$$u_L = u_{mL} + \delta u_L. \tag{26}$$

Furthermore, in practical situations, the measured displacement is known on a discrete and, most often, regular grid, and it is corrupted by noise. Consequently, the integrals in equations (18), (21) and (22) are discretized on a set of N points, $(x_i)_{i=1..N}$, representing the displacement measurement locations, with $\Delta x_i = L/N$ the size of each "pixel". We then define the *discrete least square identification functional* for a given testing situation $Z \in \mathcal{T}$ and spatial discretization, N:

$$\widetilde{F}(\theta;Z) = \frac{1}{2}\sum_{n=1}^{N} |u(\theta;Z)(x_i) - \widetilde{u}_m(x_i)|^2 \Delta x_i. \tag{27}$$

The noisy displacement at each measurement point, $\widetilde{u}_m(x_i)$, verifies

$$\widetilde{u}_m(x_i) = u_m(x_i) + \delta_u(x_i). \tag{28}$$

The statistical properties of the random variable $\delta_u(x)$ depend on the characteristics of the measurement apparatus. We suppose that this variable follows a centered, Gaussian distribution with standard deviation σ_{δ_u}. Finally, the error on the boundary condition, δu_L, is expressed as a fraction ($\epsilon \geq 0$) of the measurement error

$$\delta u_L = \epsilon \delta_u(L). \tag{29}$$

Let us remark that, in this particular case, $\widetilde{F}(\theta;Z)$ is then a real valued function of two real variables $\theta = (\mu,\xi)$. It is thus possible to plot its variations in the form of level curves to investigate its convexity in the vicinity of the true viscoelastic property values $\theta_m = (\mu_m,\xi_m)$. In what follows, we will study the sensitivity of the identification procedure with respect to:

- **Material properties**
- Shear stiffness: μ.
- Damping ratio: ξ.

- **Discretization**
- Wave discretization: the ratio λ/L, describing the wavelength in relation to the size of the geometry.
- Spatial discretization: N, defining the spatial resolution of the measurements and the numerical approximation of $F(\theta;Z)$ as $\widetilde{F}(\theta;Z)$.
- **Noise**
- Measurement noise: σ_{δ_u}
- Bias on the boundary condition: ϵ.

2.4 | Definition of the numerical study configurations

To characterize the sensitivity of the objective function, $\widetilde{F}$, defined in Equation (27) with respect to the parameters outlined above in Section 2.3, a Monte-Carlo type approach based on displacement fields provided by the analytic solution given by Equation (15). A generic problem domain was developed, with $L=1$, $u_L=L/1000$, and $\omega=2\pi 1 rad/s$. In this study the pulsation ω and the mass density ρ are kept constant so that varying the shear stiffness μ is equivalent to varying the elastic wavelength λ. The ratio $\frac{\lambda}{L}$ was then varied from 40% to 400%. To study a range of conditions from several wave periods present in the domain to small fractions of a wave present in the domain. The first five elastic resonance conditions, as defined in section 2.1, are encountered at $\frac{\lambda}{L}=200\%,100\%,66.67\%,50\%$ and 40%. To study the effects of sampling of the mechanical wavefield, two levels of spatial resolution where considered, $N=64$ and $N=8$, where $N=64$ ensures over 25 sampling points for one wave at the shortest wavelength, $\frac{\lambda}{L}=40\%$, while $N=8$ provides 3 measurements *per* period for these shortest waves. In parallel, the damping ratio, ξ was varied from 0% to 10%, a range indicative of biological tissue.[30] For the Monte-Carlo study, 2000 identifications for the storage and loss modulus indicated in Equation (2) were performed, with μ and ξ then defined by Equation (7) and Equation (8). These identifications were performed based on the minimization of F via the Matlab function *fmincon* (*version 2021b, The MathWorks, Inc.; Natick MA, USA*). Each of these identifications was performed with a unique initial material parameter estimate, $C_0=A_0+jB_0$, where A_0 and B_0 varied randomly within a range of 25% of the true property values for the given configuration to investigate the sensitivity of the minimization of the objective function F with respect to the initial property estimate. The default *interior point* algorithm for *fmincon* was used, with the lower constraint: $A>0;B>0$. In addition, two states of Gaussian measurement noise were considered, $\sigma_{\delta_u}=0\%$ and $\sigma_{\delta_u}=10\%$, where the percentage was calculated in reference to the maximum displacement amplitude within the domain. The bias generated by noise within the boundary conditions applied for identification was studied by considering the two following situations: $\varepsilon=0\%$, where the applied boundary conditions are known perfectly; and $\epsilon=100\%$, where the boundary conditions are known only at the level of measurement uncertainty.

2.5 | Ethical statement

No part of this work involved the use of human or animal subjects, and thus the research presented here was not subject to consideration by the Institutional Review Board (IRB) of any of the authors' affiliated institutions.

3 | RESULTS

Here, we present three groups of results: firstly, a selection of analytic solutions, $u(x)$, (15) is given for a range of mechanical properties representative of biological tissue and typical elastography test conditions[30]; secondly, graphic representations of the objective function F for a more comprehensive selection of material properties are presented; and finally, a synthesis of the Monte-Carlo experiments described in Section 2.4 is provided for a range of experimental conditions that cover most practical elastography configurations.

3.1 | Viscoelastic wave solutions and measurements

Analytic solutions of (15) are given for a selection of cases covering a range of experimental conditions for different elastography configurations. Figure 1 shows the analytic solutions for a selection of material parameters corresponding

to mechanical wavelengths λ/L covering 50%–325% of the measurement domain with a damping ratio of 1%. These cases illustrate situations where: the mechanical wavelength is shorter than the measurement domain ($\lambda/L = 50\%$); the mechanical wavelength is longer the measurement domain but the domain still covers more than 50% of the wavelength ($\lambda/L = 137.5\%$); the measurement domain covers less than 50% of the wavelength ($\lambda/L = 212.5\%$); and finally the measurement domain covers just over 25% of the wavelength ($\lambda/L = 350\%$). Figure 2 shows the same selection of wavelengths but with a higher damping ratio, $\xi = 10\%$.

In a typical elastography experiment, the boundary conditions used for model based inversion methods are taken from the measured displacements. Figure 3 illustrates the bias generated by the use of noisy boundary conditions by comparing the true reference solution, for the case of $\lambda/L = 50\%$ and $\xi = 10\%$, to a biased solution determined with the same material parameters with noisy boundary conditions. To generate this biased solution, Gaussian noise (at 10% of the maximum displacement value) was added to the reference solution. The displacement values at $x = L$ where then used as the applied boundary conditions for the final, biased solution, shown in *magenta* and *cyan* in Figure 3. Note that the scaling in Figure 2 is different from the one used in Figure 3 in order to better evidence the modifications in the displacement values due to the introduction of the noise in the boundary conditions.

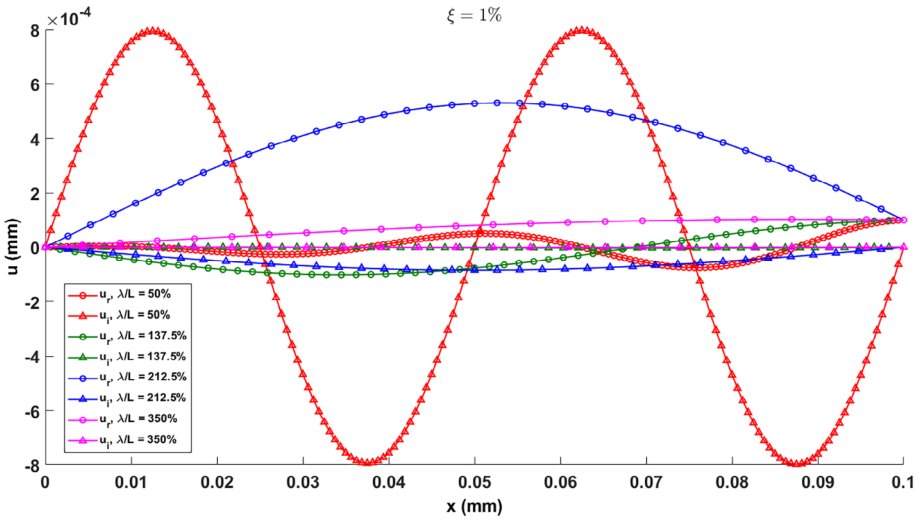

FIGURE 1 A single analytic displacement solutions (real part u_r and imaginary part u_i) for $\xi = 1\%$ with the configurations: $\lambda/L = 50\%$, 137.5%, 212.5%, and 350%.

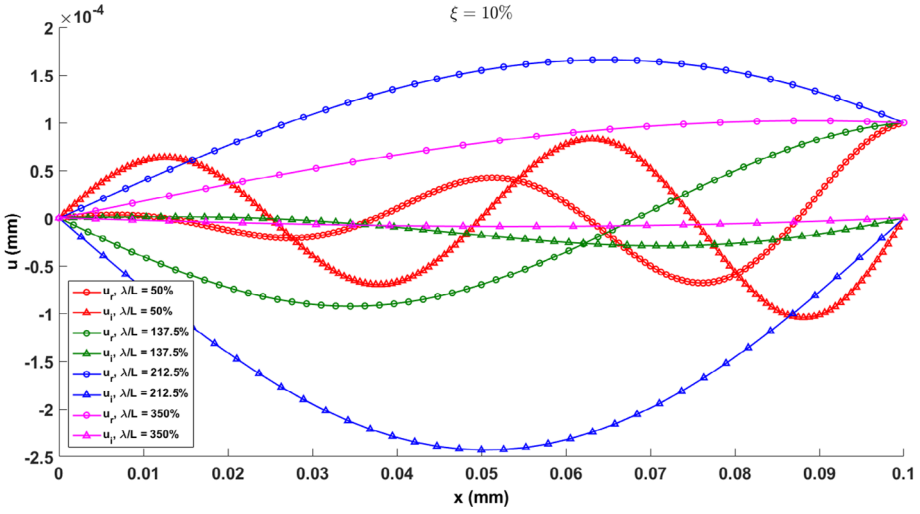

FIGURE 2 The analytic displacement solution (real part u_r and imaginary part u_i) for $\xi = 10\%$ with the configurations: $\lambda/L = 50\%$, 137.5%, 212.5%, and 350%.

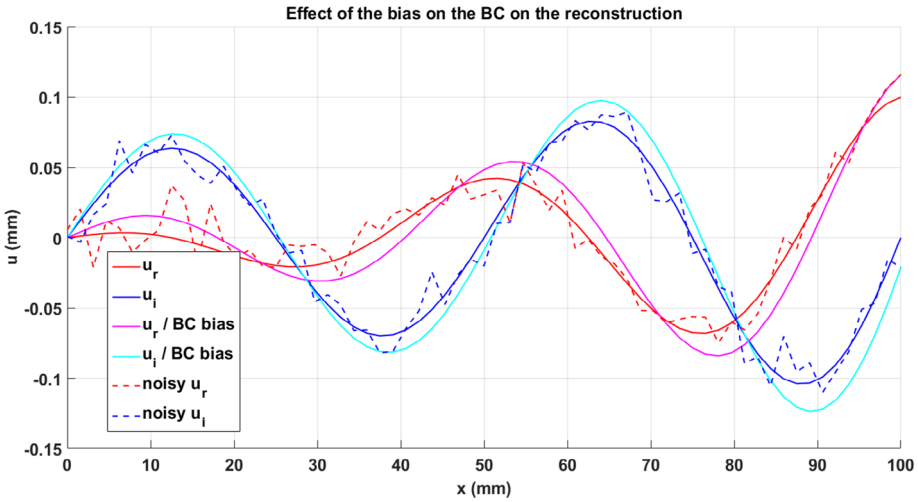

FIGURE 3 The analytic displacement solution (real part u_r and imaginary part u_i, configuration: $\lambda/L = 50\%$ and $\xi = 10\%$) compared to the case where 10% noise is applied (dashed lines). Additionally, the model solution computed with noisy boundary conditions is shown (magenta and cyan).

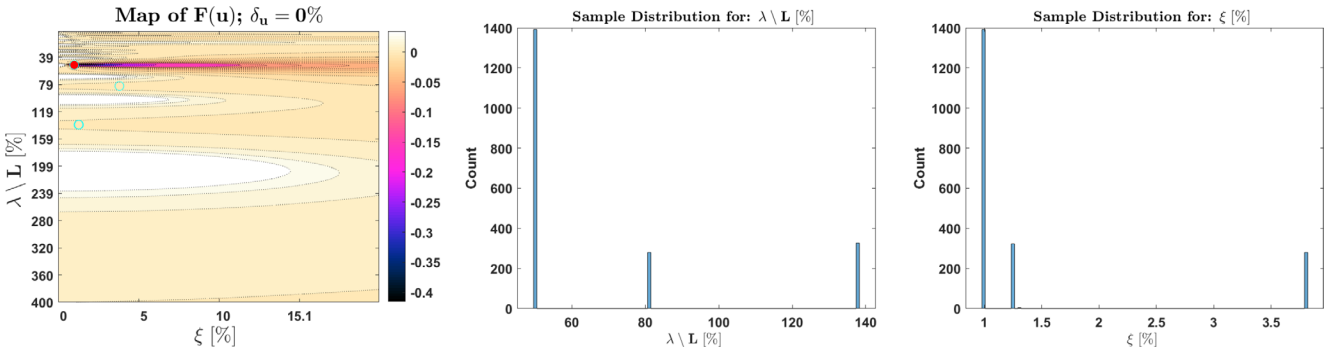

FIGURE 4 The map of the noiseless cost function, $F(\theta;Z)$ (left), with the distribution of identified properties $(\lambda/L,\xi)$ (left, *cyan* circles) or in histogram form (center and right), for the case of $\lambda/L = 50\%$; $\delta_u = 0\%$; $N = 8$; $\xi = 1\%$; and $\delta_L = 0\%$. The reference properties are indicated by the *red* circle (left).

3.2 | Objective function maps for specific wave conditions

Figures 4–12 illustrate the surface of the discrete objective function, $\widetilde{F}(\theta;Z)$, given by Equation (27), in the plane $(\lambda/L,\xi)$, which is better suited for direct mechanical interpretation as it separates the viscoelastic wavelength and attenuation effects. A selection of illustrative mechanical configurations is presented, showing the effects of the varied parameters: N, λ/L, ξ, σ_{δ_u}, and ϵ. For each instance of a reference mechanical configuration, the position of all sets of the identified viscoelastic material properties from the Monte-Carlo study described in section 2.4 are shown as *cyan* circles. The statistical distribution of the identified properties are illustrated in the histograms deduced from the final results of the identification process.

Figures 4–6 illustrate three populations of identified properties in a case of low mechanical attenuation and thus significant resonance effects. Even in the absence of measurement noise $(\delta_u = 0\%)$ or the absence of noise in the applied boundary conditions, $(\delta_L = 0\%)$, identification results for this mechanical configuration show three distinct solution populations in both the illustrated cost function plots and in the histogram distributions.

Figures 7–12 all show cases of increased mechanical attenuation, $\xi = 10\%$. Resonance effects are less significant in these cases and only one population of identified properties is observed in the cost function plots and histogram distributions.

Figures 7–9 compare two different experimental configurations, $\delta_L = 0\%$ vs. $\delta_L = 100\%$ and $N = 8$ vs. $N = 64$ for the case of $\lambda/L = 50\%$. Figures 7 and 8 show the effects of noise in the applied boundary conditions on the distribution of

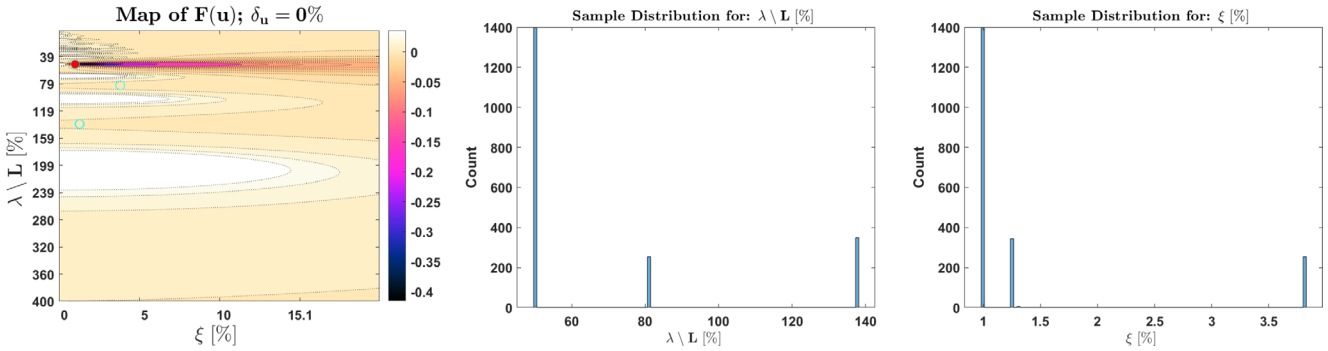

FIGURE 5 The map of the noiseless cost function, $F(\theta;Z)$ (left), with the distribution of identified properties $(\lambda/L,\xi)$ (left, *cyan* circles) or in histogram form (center and right), for the case of $\lambda/L=50\%$; $\delta_u=0\%$; $N=64$; $\xi=1\%$; and $\delta_L=0\%$. The reference properties are indicated by the *red* circle (left).

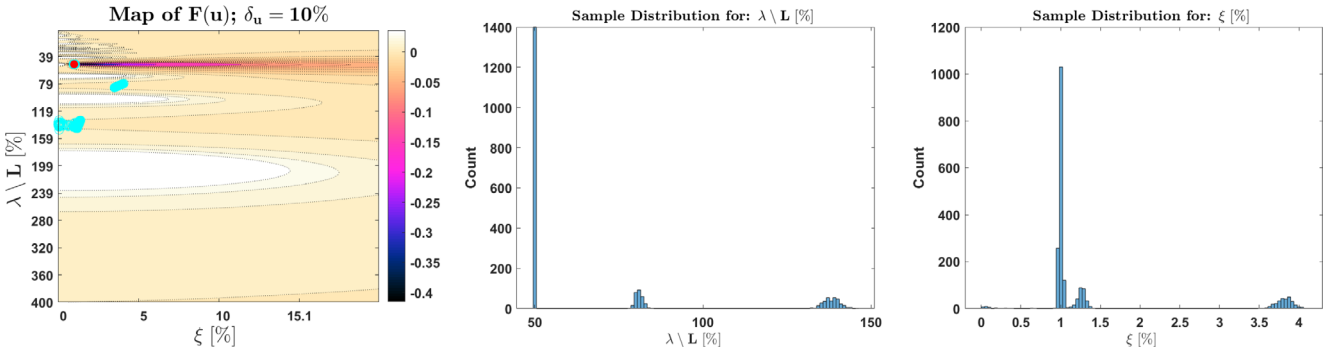

FIGURE 6 The map of the noiseless cost function, $F(\theta;Z)$ (left), with the distribution of identified properties $(\lambda/L,\xi)$ (left, *cyan* circles) or in histogram form (center and right), for the case of $\lambda/L=50\%$; $\delta_u=10\%$; $N=64$; $\xi=1\%$; and $\delta_L=0\%$. The reference properties are indicated by the *red* circle (left).

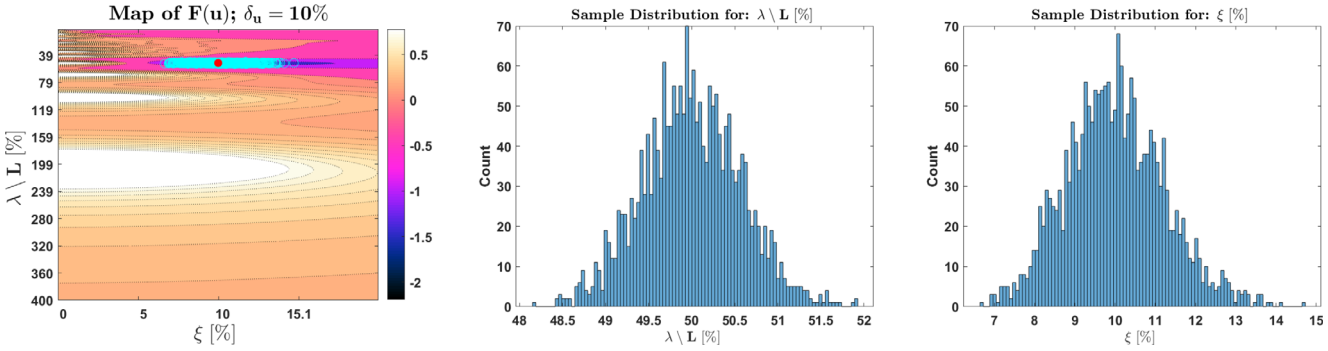

FIGURE 7 The map of the noiseless cost function, $F(\theta;Z)$ (left), with the distribution of identified properties $(\lambda/L,\xi)$ (left, *cyan* circles) or in histogram form (center and right), for the case of $\lambda/L=50\%$; $\delta_u=10\%$; $N=8$; $\xi=10\%$; and $\delta_L=100\%$. The reference properties are indicated by the *red* circle (left).

reconstructed material properties, while Figures 7 and 9 show the impact of increased measurement density on the identified property distributions.

Figure 10 shows a typical identification result in the case of higher mechanical attenuation, $\xi=10\%$, with less than one mechanical wavelength in the measurement domain, $\lambda/L=137.5\%$, at a non-resonant frequency. Again, a unique identification population is observed. Note that the sample population for the ξ distribution is slightly asymmetric,

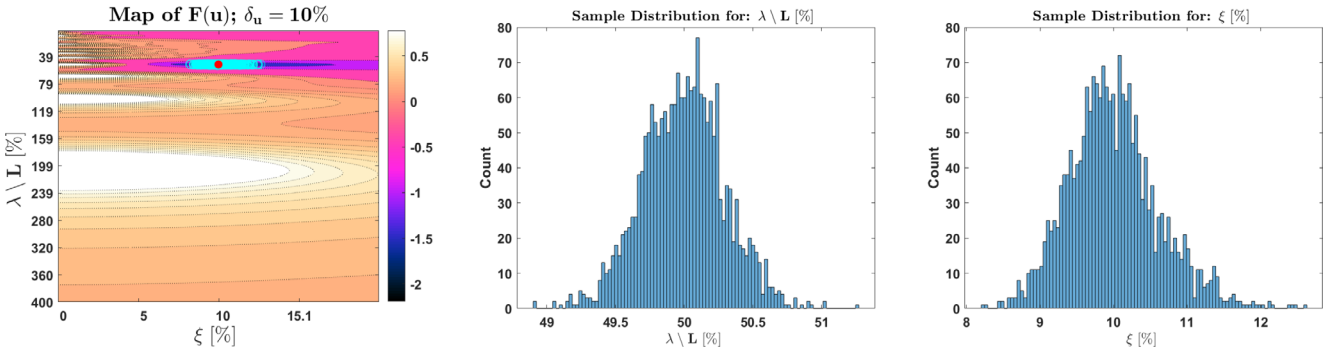

FIGURE 8 The map of the noiseless cost function, $F(\theta;Z)$ (left), with the distribution of identified properties $(\lambda/L,\xi)$ (left, *cyan* circles) or in histogram form (center and right), for the case of $\lambda/L = 50\%$; $\delta_u = 10\%$; $N = 8$; $\xi = 10\%$; and $\delta_L = 0\%$. The reference properties are indicated by the *red* circle (left).

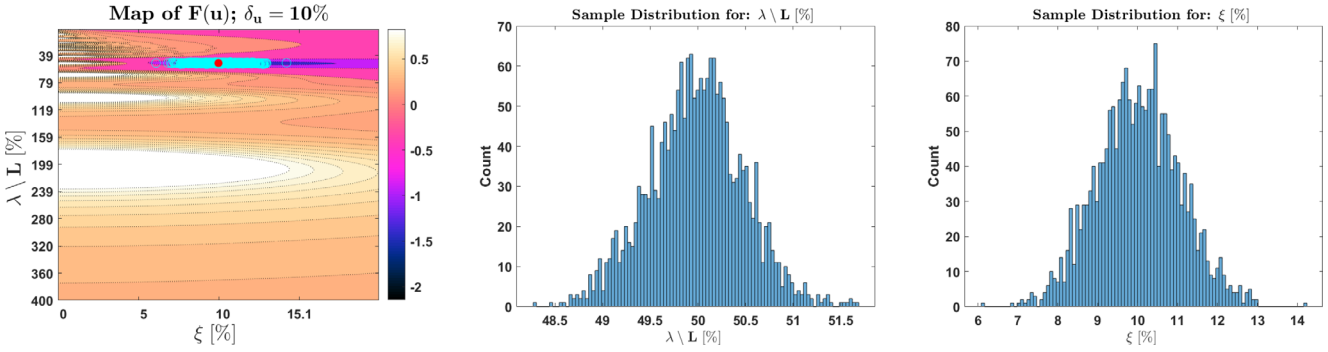

FIGURE 9 The map of the noiseless cost function, $F(\theta;Z)$ (left), with the distribution of identified properties $(\lambda/L,\xi)$ (left, *cyan* circles) or in histogram form (center and right), for the case of $\lambda/L = 50\%$; $\delta_u = 10\%$; $N = 64$; $\xi = 10\%$; and $\delta_L = 100\%$. The reference properties are indicated by the *red* circle (left).

and thus non-Gaussian, due to the visually notable asymmetry of the objective function around its minimum in the ξ direction.

Figures 11 and 12 show the challenging case where the measurement domain only covers approximately one-third of the mechanical wavelength, $\lambda/L = 350\%$. In the case where noise is present in both the measurements and the applied boundary conditions, Figure 11 shows that the identification is very poor, as can be seen by the extent of the of the variation in both the λ/L and ξ distributions. Precise identification of the material properties in this case is essentially impossible. Figure 12, however, shows that removal of the noise on the applied boundary conditions allows sufficient regularization of the problem to obtain a coherent distribution of identification results distributed around the true mechanical properties, albeit with relatively high variance.

3.3 | Property characterization performance across a range of wave conditions

Figures 13–18 introduce several performance indicators that summarize the quality of the characterizations shown in Figures 4–12 across the range of mechanical properties and experimental conditions used in the Monte-Carlo study outlined in Section 2.4. To avoid the problem of statistical outliers, we analyze the characterization results on the population corresponding to the 5–95*th* percentile, in terms of error with respect to the storage modulus, A, of the Monte-Carlo study population. We introduce three types of performance indicators: systematic errors represented by the mean error for the 5–95*th* percentile; random errors represented by the variance of the same 5–95*th* percentile; the quality of the non-linear minimization via the mean value of the cost function; and the convergence speed via the number of iterations to complete the minimization. Each figure is shown as a map in the plane of $(\lambda/L,\xi)$. The first row of images shows the systematic error for the viscoelastic properties A (*left*) and B (*right*), as a percentage of the reference value

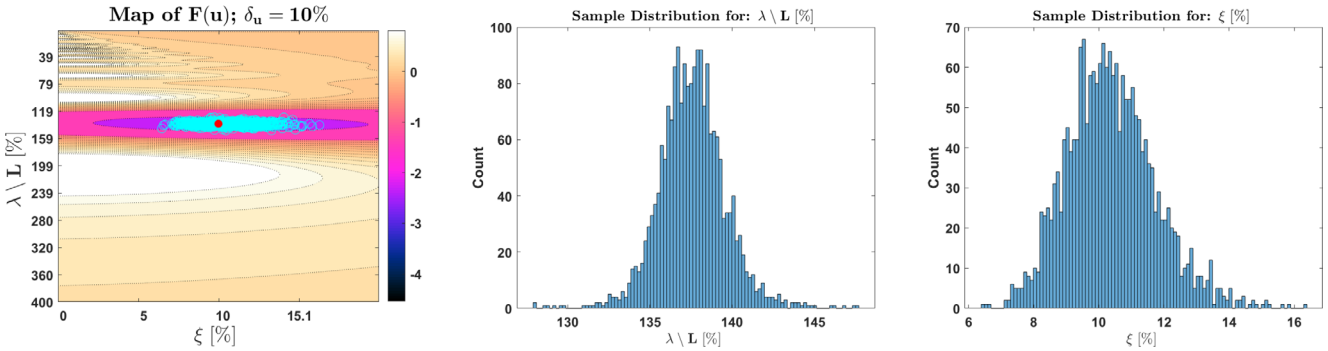

FIGURE 10 The map of the noiseless cost function, $F(\theta;Z)$ (left), with the distribution of identified properties $(\lambda/L,\xi)$ (left, *cyan* circles) or in histogram form (center and right), for the case of $\lambda/L=137.5\%$; $\delta_u=10\%$; $N=64$; $\xi=10\%$; and $\delta_L=100\%$. The reference properties are indicated by the *red* circle (left).

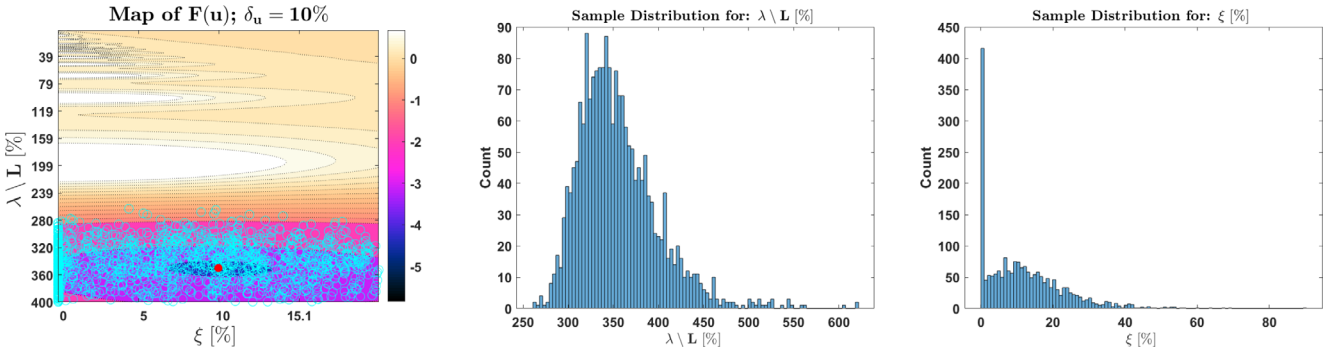

FIGURE 11 The map of the noiseless cost function, $F(\theta;Z)$ (left), with the distribution of identified properties $(\lambda/L,\xi)$ (left, *cyan* circles) or in histogram form (center and right), for the case of $\lambda/L=350\%$; $\delta_u=10\%$; $N=64$; $\xi=10\%$; and $\delta_L=100\%$. The reference properties are indicated by the *red* circle (left).

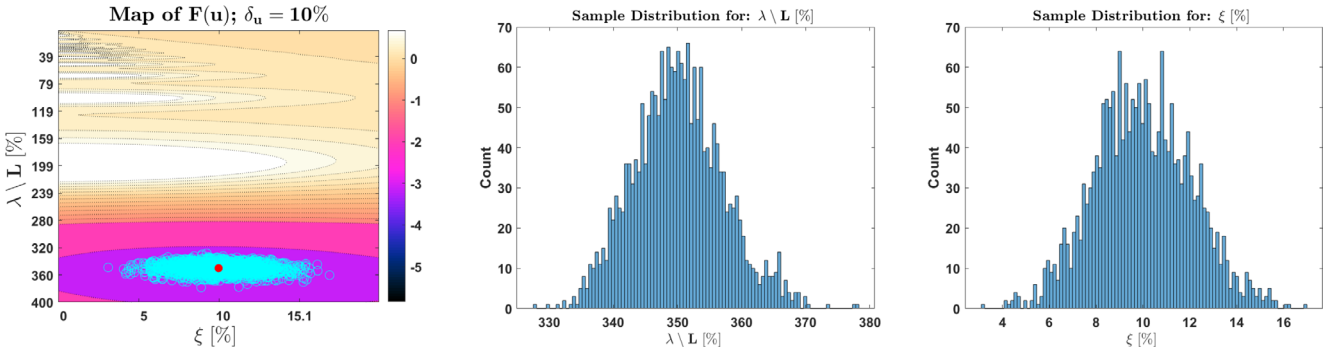

FIGURE 12 The map of the noiseless cost function, $F(\theta;Z)$ (left), with the distribution of identified properties $(\lambda/L,\xi)$ (left, *cyan* circles) or in histogram form (center and right), for the case of $\lambda/L=350\%$; $\delta_u=10\%$; $N=64$; $\xi=10\%$; and $\delta_L=0\%$. The reference properties are indicated by the *red* circle (left).

displayed on a *logarithmic* scale (base 10). The second row of images for each figure shows the random errors for the viscoelastic properties A (*left*) and B (*right*), again as a percentage of the reference value on a base 10 *logarithmic* scale. Finally, the third row of images for each figure indicates the convergence speed of the identification as the average number of minimization iterations, N_{iter} (*left*) and the quality of the minimization as the average value of the cost function, F (*right*).

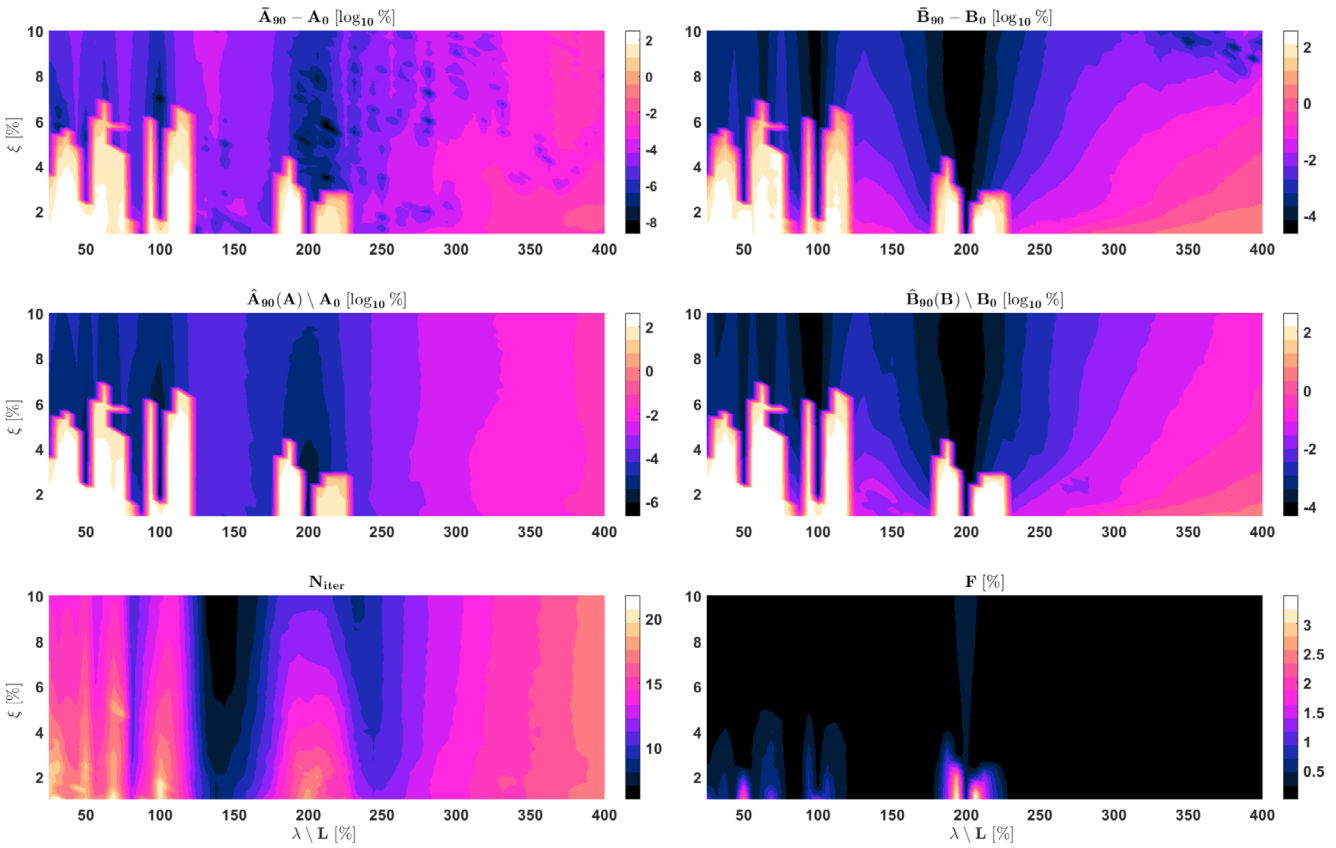

FIGURE 13 Property characterization performance indicators for the configuration: $N = 64$; $\delta_u = 0\%$; $\delta_L = 0\%$. First row: systematic error for A (*left*) and B (*right*). Second row: random errors for A (*left*) and B (*right*). Third row: convergence speed (N_{iter}) (*left*) and quality of the minimization (F) (*right*).

Figure 13 shows the summarized results for the case of $N = 64$ measurements within the domain, with no measurement noise, $\delta_u = 0\%$. This represents the nearly perfect identification case, with an ample number of measurements along the mechanical wavelength and perfect measurements of the displacement field (i.e., no noise). Even in this case, we see that not all instances of different initial conditions succeed in identifying the correct reference values for A and B. Notably, we see that for low attenuation cases $\xi < 7\%$, regions of large identification error and variance are observed for relative stiffness values corresponding to resonance cases ($\lambda/L = 200\%, 100\%, 66.67\%, 50\%, 40\%$). These regions correspond to cases where the objective function is highly non-convex due the presence of resonance peaks, leading to multiple populations of solutions centered in different valleys of the objective function (see, e.g., Figures 4–6). We also observe, for cases where $\lambda/L > 200\%$, that the mean and variance of the identification error increase progressively with λ/L, indicating that identification becomes less and less feasible as the wave content within the measurement domain decreases. Conversely, for the cases with sufficient wave content within the domain ($\lambda/L < 200\%$) and sufficient attenuation ($\xi > 7\%$) the mean identification error and variance remain small and are mostly independent of ξ for fixed λ/L. The results of the third row of images confirm the trends observed in the mean identification error and variance results, where regions of mechanical resonance require a larger number of iterations for convergence and the final objective function values are larger than those observed in non-resonant cases. The one notable exception to this correspondence is found in the objective function values in the case where $\lambda/L > 200\%$ (third row, right column). In these instances, we see that the final objective function values are relatively low, despite large errors in the identification of the mechanical properties. This is a result of the relatively flat topology of the objective function in these cases (see, e.g., Figures 11 and 12), where a large variation in the mechanical properties still falls within the basin surrounding the objective function's true minimum.

Figures 14 and 15 show similar tendencies for the case of increased measurement noise ($\delta_u = 10\%$), with or without boundary noise ($\delta_L = 0\%$ *or* 100%). While Figures 16 through 18 show overall similar behavior even with decreased spatial resolution of the displacement measurements, $N = 8$. In all these cases, Figures 13–18 provide quantitative

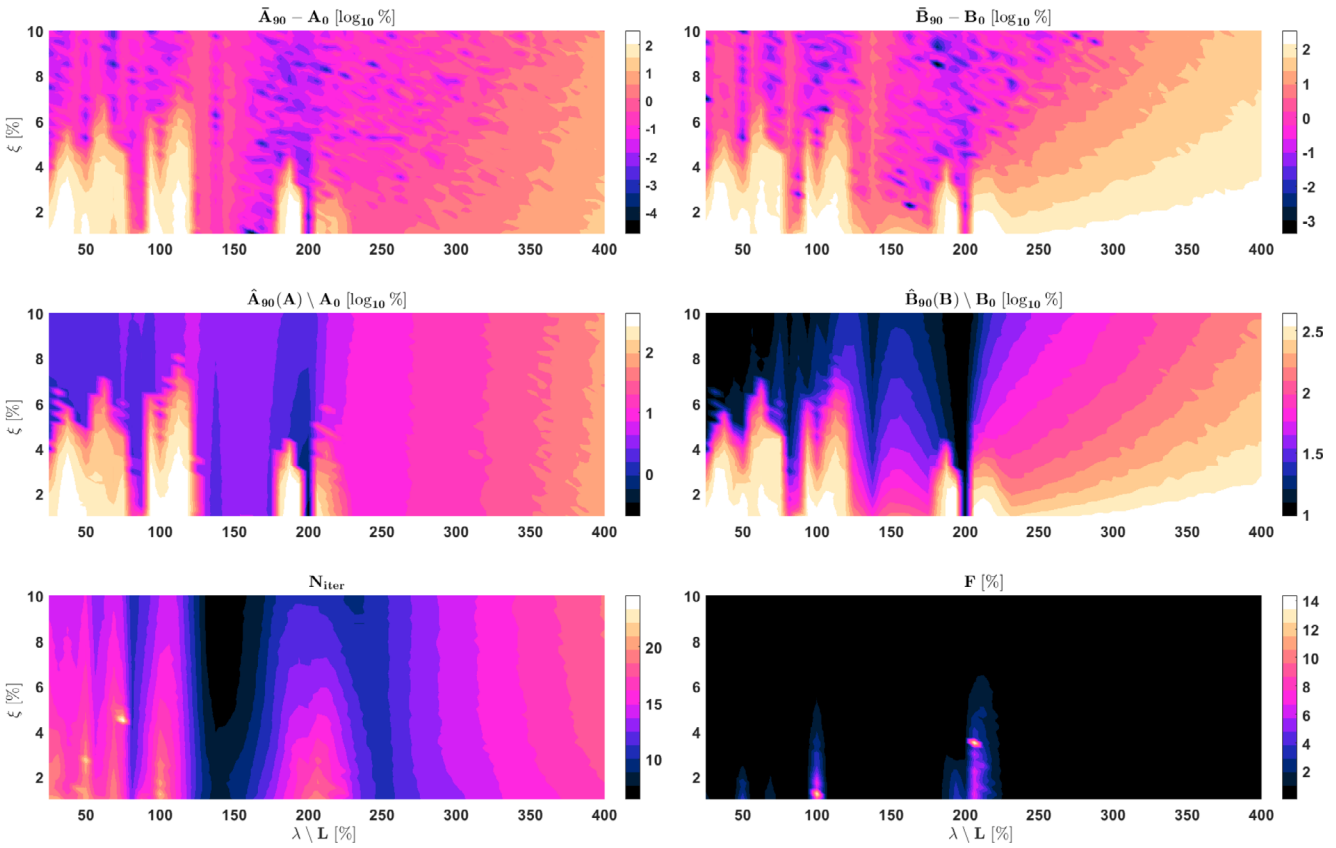

FIGURE 14 Property characterization performance indicators for the configuration: $N = 64$; $\delta_u = 10\%$; and $\delta_L = 100\%$. First row: systematic error for A (*left*) and B (*right*). Second row: random errors for A (*left*) and B (*right*). Third row: convergence speed (N_{iter}) (*left*) and quality of the minimization (F) (*right*).

indicators for the expected error and variance of the identification problem for the prescribed mechanical and experimental conditions.

4 | DISCUSSION

In addition to providing closed form expressions for the displacement field u and the cost function F (in specific cases, see Section 2.2.1), the analytic solution to the viscoelastic wave equation presented in Section 2.1 facilitates rapid evaluation of the mechanical property identification process through characterization of the associated cost function.[27] This solution also significantly accelerated the Monte-Carlo investigation of the performance of the property characterization problem for a wide range of experimental conditions, as described in Section 2.4. Overall, we see that the accuracy of mechanical property identification depends not only on measurement noise and resolution, but also, for a given measurement domain, on the mechanical behavior itself. We present some specific observations based on the study results presented above, in what follows we will focus principally on the effects of: resonance, dimension of the measurement domain with respect the wavelength, noise and boundary conditions.

4.1 | Resonance

As expected, resonance plays an important role in identification, but its impact is reduced as mechanical attenuation increases. Figures 13–18 clearly show the effects of resonance on the ability to correctly identify the storage and loss modulus for damping ratio levels up to $\xi = 5\% - 6\%$. Figures 6 and 7 show two examples of this effect in the specific case of mechanical property identification at a resonance point. Separate solution populations arise in the case of resonance peaks in low attenuation materials ($\xi = 1\%$). We see that resonance creates peaks in the objective function and,

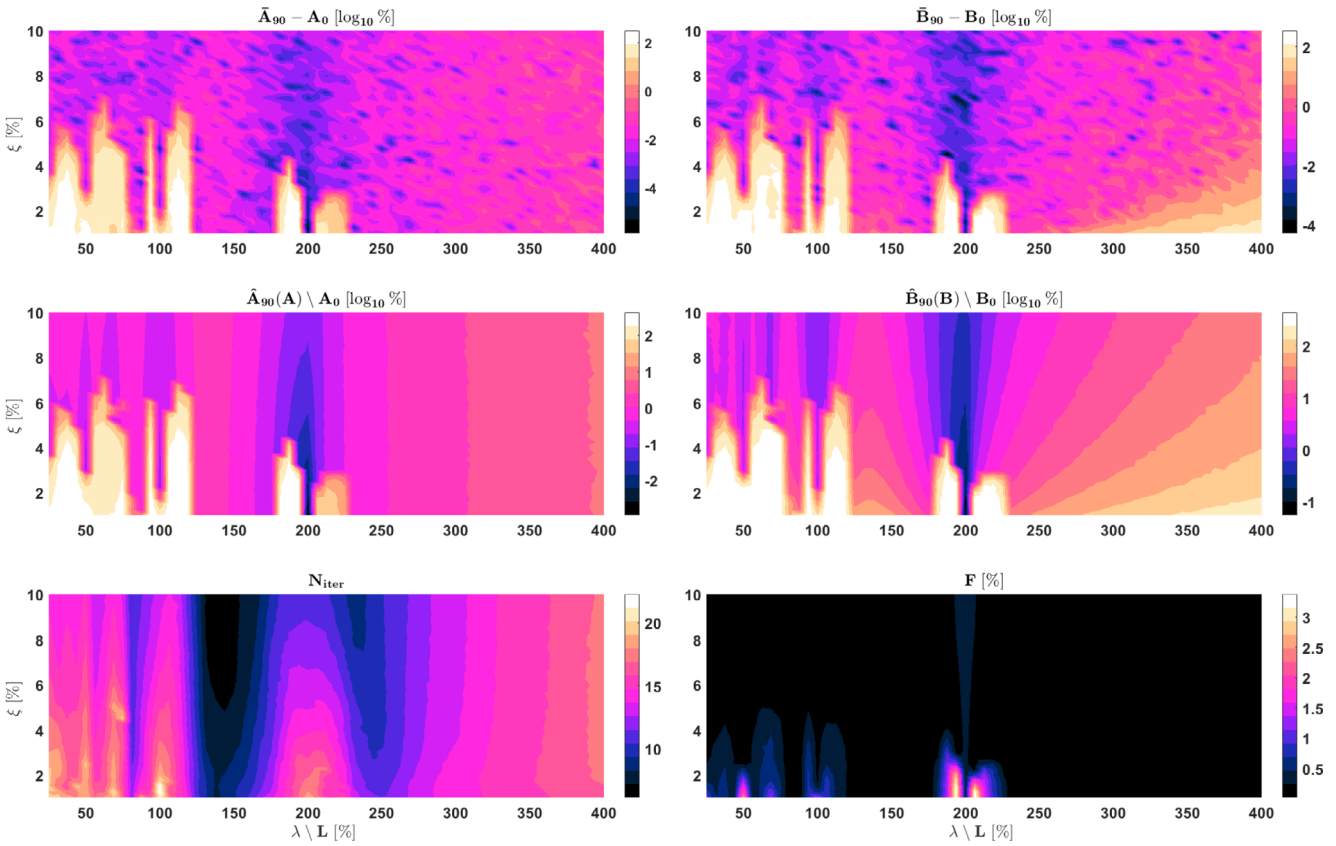

FIGURE 15 Property characterization performance indicators for the configuration: $N = 64$; $\delta_u = 10\%$; and $\delta_L = 0\%$. First row: systematic error for A (*left*) and B (*right*). Second row: random errors for A (*left*) and B (*right*). Third row: convergence speed (N_{iter}) (*left*) and quality of the minimization (F) (*right*).

for different noise instances, leads to local minima in valleys between different resonance conditions (see the map of $F(\theta;Z)$ on the left of Figure 6). These local minima are discovered due to the random variation of the initial guess for the minimization problem used in the Monte-Carlo approach for this study. In these cases, Figures 4–6 show that between 60% and 70% of the identifications fall within the population corresponding to the reference properties, for this specific configuration. However, at higher attenuation levels ($\xi = 10\%$), these resonance peaks function like constraints which restrain the stiffness estimate to a relatively narrow distribution around the reference properties, thus reducing the variance observed in these identifcations (as seen in the middle row of graphics in Figures 13–18, e.g., for λ/L around 200%).

For the case of identification away from resonance points, Figures 13–18 show that, for λ/L below roughly 120%, property identification at attenuation levels below $\xi = 5\% - 6\%$ is heavily affected by the presence of local minima, as discussed above and depicted in Figures 4 to 6. For λ/L between roughly 120% and 180% however, there is a relatively uniform band where identification can be achieved consistently at almost any attenuation level, at the cost of slightly higher variation. Figure 10 provides a good demonstration of this case, where we see that local minima are not present, but that the constraining effect of neighboring resonance valleys in the objective function is not present either, leading to wider distributions of estimated properties around the reference properties.

4.2 | Domain dimension versus Wavelength

Figures 13–18 show clearly that identification of the true mechanical properties becomes difficult as the wavelength increases above 200% of the domain, similar to the Abbe diffraction limit in optical imaging. Mechanical properties can be identified above this limit, albeit with high levels of variance, but in general this requires special treatment of the

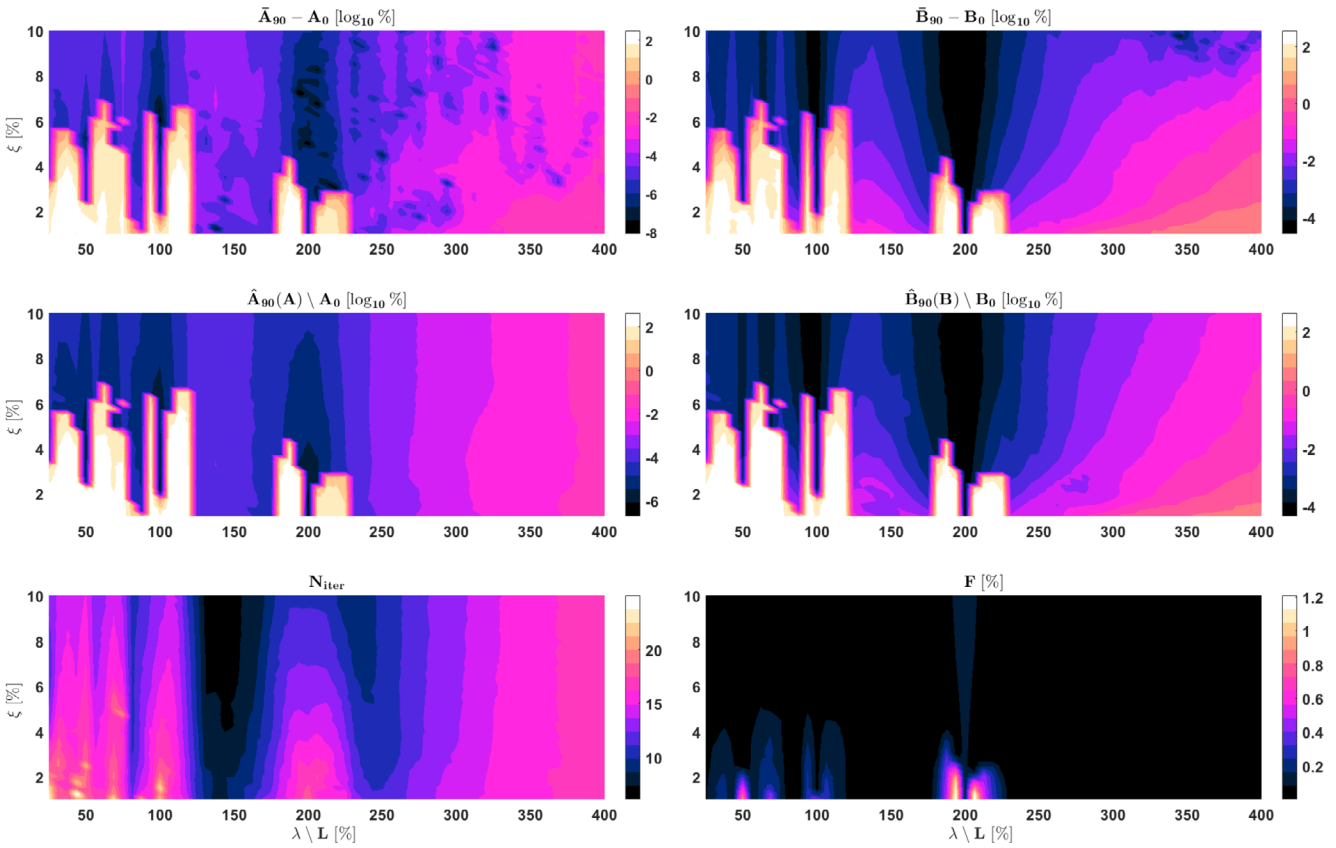

FIGURE 16 Property characterization performance indicators for the configuration: $N = 8$; $\delta_u = 0\%$; and $\delta_L = 0\%$. First row: systematic error for A (*left*) and B (*right*). Second row: random errors for A (*left*) and B (*right*). Third row: convergence speed (N_{iter}) (*left*) and quality of the minimization (F) (*right*).

identification problem (e.g., removing measurement noise on the boundary, i.e., $\delta_L = 0\%$, as demonstrated in Figures 11 and 12).

Equations (9) and (23) show us that stiffness, μ, and attenuation, ξ, appear in combination within the cost function, $F(\theta; Z)$. This leads to a possible covariance between these two terms such that overestimating the stiffness leads to an overestimation of attenuation in the domain. This covariance appears more pronounced at higher values of λ/L and can be observed in the different specific instances of the cost function shown in Figures 10–12, where the principal axis of the ellipse surrounding to the objective function minimum is seen to descend to the right.

4.3 | Noise and boundary conditions

Noise within the measurement domain has the expected result of increasing the variance within the population of identified property values, but, for non-resonant cases where λ/L is sufficiently low, the presence of noise does not significantly change the nature of the identification result. In the case of resonance, the presence of measurement noise can lead to the appearance of multiple solution populations, which can, in turn, lead to a rapid increase in the variance of the identified properties values.

Errors in the boundary conditions however have a specific effect on the mechanical property identification from general measurement noise within the domain. For higher λ/L levels in particular, boundary noise has notable effect on the quality of material property identification. This is well illustrated by Figures 11 and 12, where the identification can introduce a correlation between the two properties, λ and ξ.

These effects are generalized for a range of λ/L values in Figures 13, 14 and 15, which show the increases in both systematic and random errors with the increase of measurement noise. Remarkably, in noisy situations ($\delta_u = 10\%$), suppressing noise in the boundary conditions ($\delta_L = 0\%$) can decrease the identification error by an order of magnitude.

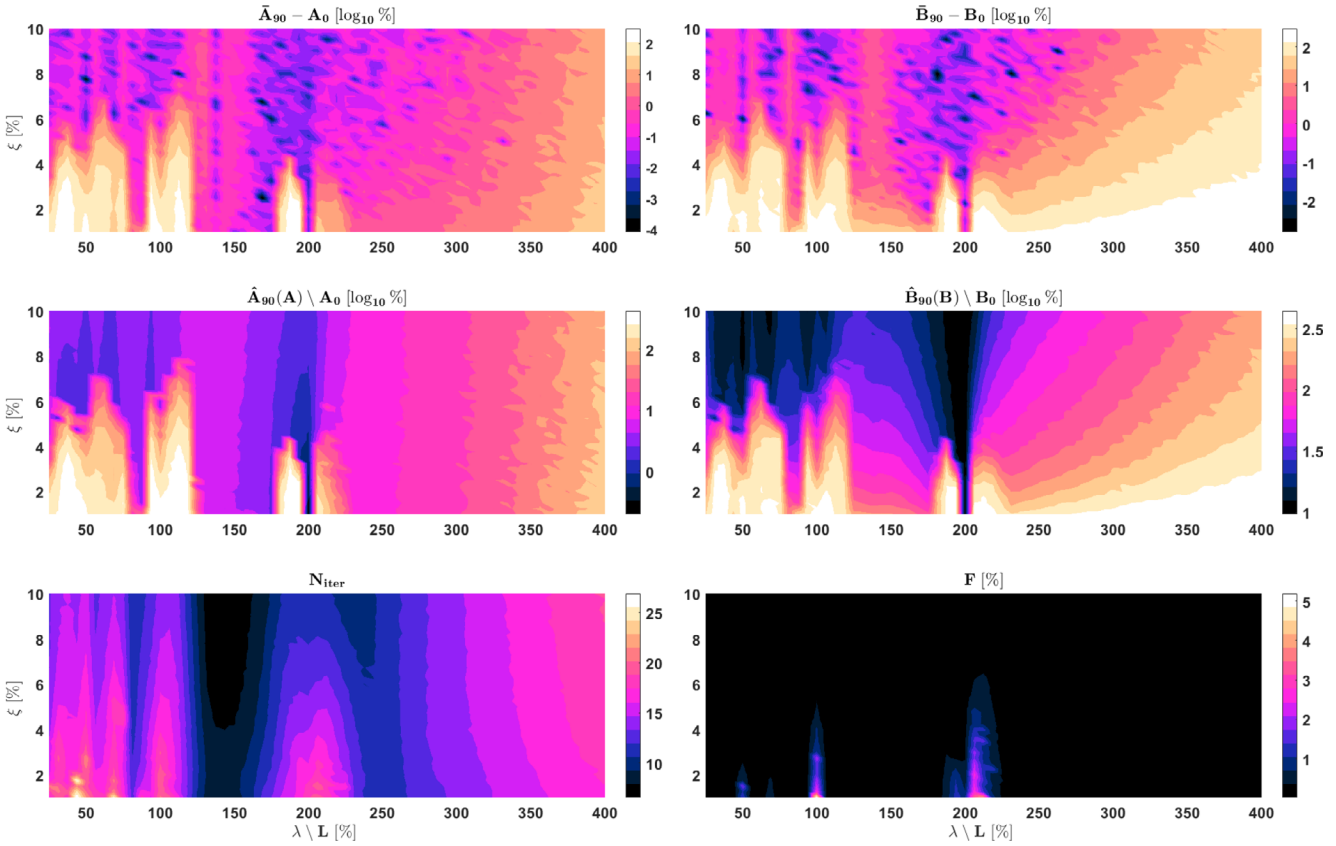

FIGURE 17 Property characterization performance indicators for the configuration: $N = 8$; $\delta_u = 10\%$; and $\delta_L = 100\%$. First row: systematic error for A (*left*) and B (*right*). Second row: random errors for A (*left*) and B (*right*). Third row: convergence speed (N_{iter}) (*left*) and quality of the minimization (F) (*right*).

4.4 | Translation of 1D analysis to 3D

In terms of translating these 1D observations to 3D, a few factors should be kept in mind. First of all, the characteristic length of a 1D system, L, will be stretched in *isotropic* 3D cases by a factor of $\sqrt{3}$, as wave propagation along the diagonal becomes possible. The critical ratio of λ/L would thus become $\lambda/\left(\sqrt{3}L\right)$, for 3D isotropic voxels of edge length L, increasing the mechanical wavelength at which viscoelastic stiffness can be characterized. The role of the damping ratio in characterization is principally related to the presence of resonance effects in the displacement data. The presence of resonance leads to local minima in the objective function which perturb the characterization process. In the 1D case observed here, the impact of these resonance effects was essentially eliminated for values $\xi > 0.07$. In 3D cases, resonance effects may be more prominent due to the presence of multiple resonance modes within the system, but in principle the mechanical attenuation due to the damping ratio should have the same spatial impact, we should thus expect the damping levels necessary for accurate characterization to either increase or remain the same. In terms of boundary noise, the surface-to-volume ratio for any object is proportional to $1/L$ for any dimension, so there should not be dramatic shifts in the behavior observed here. However, for an isotropic cube, this ratio is 3 times greater than the 1D case, so we could imagine an increased impact in 3D. That said, for normally distributed noise across the surface, this increased surface-to-volume ratio should prove advantageous in averaging out the effects of noise, such that this smoothing effect would be dependent on the data resolution.

5 | CONCLUSIONS

Even in the simplified uni-dimensional framework studied here, the analytic formulation of the elastographic least-squares cost-function, $F(\theta; Z)$, is possible in the absence of noise and model error, and shows the presence of multiple

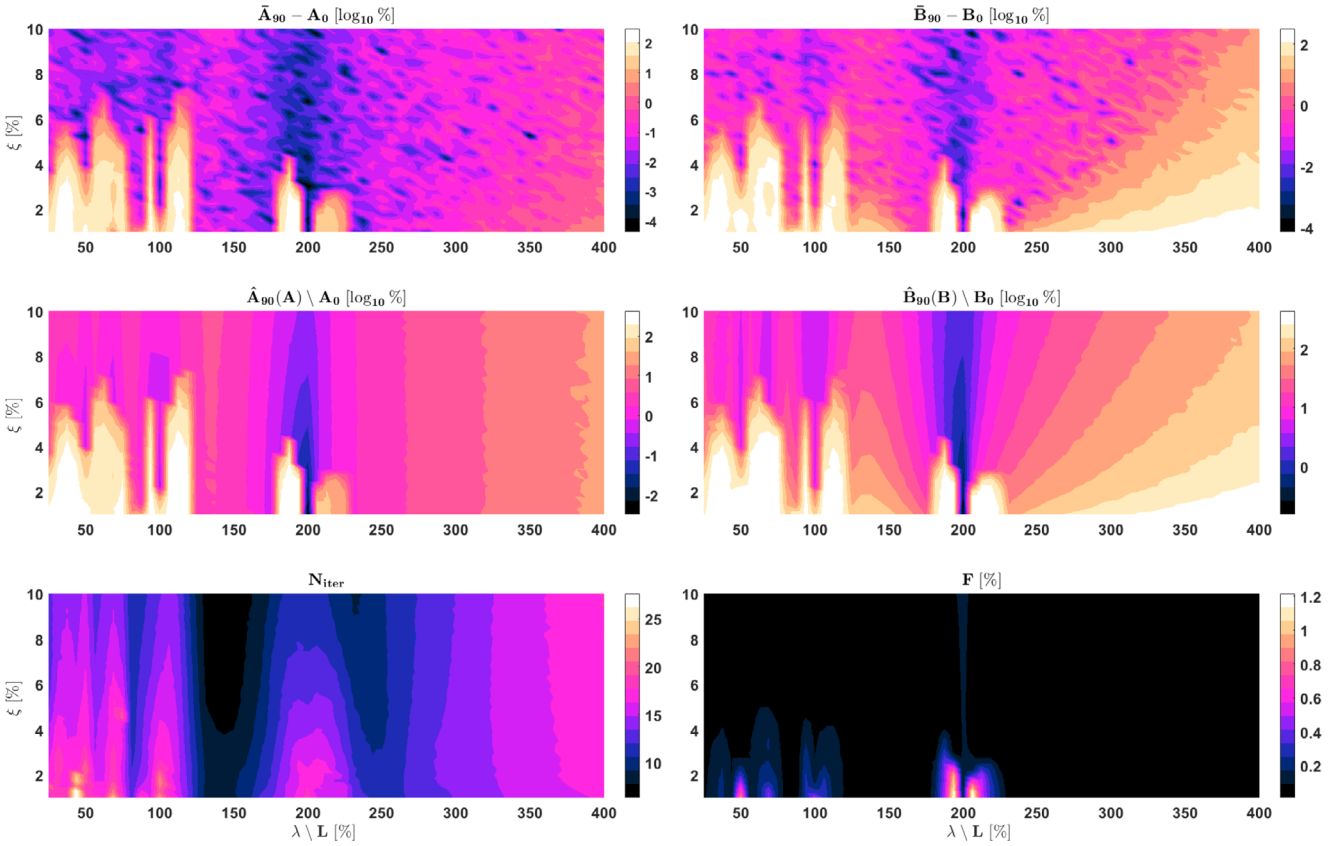

FIGURE 18 Property characterization performance indicators for the configuration: $N = 8$; $\delta_u = 10\%$; and $\delta_L = 0\%$. First row: systematic error for A (*left*) and B (*right*). Second row: random errors for A (*left*) and B (*right*). Third row: convergence speed (N_{iter}) (*left*) and quality of the minimization (F) (*right*).

solution populations due to the non-convexity of the objective function linked to resonance effects in the case of low damping, $\xi < 7\%$. While this is an important consideration for the accurate reconstruction of mechanical properties from displacement data, possibly circumvented by the use of multiple, random starting points, these effects are expected to be less important in biological tissues where damping levels are typically greater than 10%.

Another observation related to resonance effects highlighted by the Monte-Carlo study is the increased gradient in the objective function when the test conditions, Z, correspond to a resonance condition for the true mechanical properties. Here, mechanical property characterization may be more precise, as long as local minima are avoided.

In general, in particular away from resonance effects, histograms of the solution populations show that increased noise in the measured displacement field leads to increased variance in the identified properties, as expected. We have verified, but not demonstrated here, that this relationship is linear for $\lambda/L < 200\%$.

It is important to emphasize that suppression of measurement noise on the applied boundary conditions has a significant effect on the accuracy of the identified property solution. From a practical perspective, this underlines the interest in characterization methods that either allow the correction of noise on the applied boundary conditions (e.g., direct filtering) or avoid the use of measured data for the boundary conditions by introducing noiseless, intermediate fields (e.g., constitutive equation gap, coupled adjoint-state equation).

The relationship between the mechanical wavelength and size of the imaging domain, λ/L, is fundamental to the mechanical property characterization problem. In addition to the resonance effects mentioned above, identification in test conditions where the wavelength is more than twice as long as the scale at which the mechanical properties are to be estimated is difficult. Here, variance in the identified properties remains high irrespective of measurement noise, and the presence of noise in the boundary conditions can make accurate characterization impossible. Even if boundary noise has been suppressed, precise property characterization may require knowledge of the correlation between μ and ξ.

The next logical step for future analytic development is a Taylor expansion of the closed form formulation for $F(\theta;Z)$, to study the correlation between μ and ξ observed as the ratio λ/L increases.

The present work allows better understanding of the conditions in which elastic inclusions can be *characterized*, that is, the presence, position and mechanical properties can be determined for an inclusion of length $L > \frac{\lambda}{2}$, where λ is the shear wavelength within the inclusion. For future development, a differently structured study is necessary to investigate the conditions in which an elastic inclusion can be first *detected*, that is, the relationship between the inclusion length, L and the elastic contrast of the inclusion necessary for its presence and position to be perceived, without necessarily being able to characterize its true viscoelastic properties. This involves a high-dimensional Monte-Carlo study that includes parameterization of the size, elastic-contrast, and domain-discretization mismatch of the inclusion, in addition to the parameters studied here.

ACKNOWLEDGEMENT

There are no funding sources to acknolwedge for this work.

DATA AVAILABILITY STATEMENT

The data that support the findings of this study are available from the corresponding author upon reasonable request.

ORCID

Elijah Van Houten https://orcid.org/0000-0001-6565-8469

REFERENCES

1. Ormachea J, Parker KJ. Elastography imaging: the 30 year perspective. *Phys Med Biol*. 2020;65(24):24TR06. doi:10.1088/1361-6560/abca00
2. Zaitsev VY, Matveyev AL, Matveev LA, et al. Strain and elasticity imaging in compression optical coherence elastography: the two-decade perspective and recent advances. *J Biophoton*. 2021;14(2):e202000257. doi:10.1002/jbio.202000257
3. Garteiser P, Doblas S, Van Beers BE. Magnetic resonance elastography of liver and spleen: methods and applications. *NMR Biomed*. 2018;31(10):e3891. doi:10.1002/nbm.3891
4. Hiscox LV, Johnson CL, Barnhill E, et al. Magnetic resonance elastography (MRE) of the human brain: technique, findings and clinical applications. *Phys Med Biol*. 2016;61(24):R401-R437.
5. Manduca A, Bayly PJ, Ehman RL, et al. MR elastography: principles, guidelines, and terminology. *Magn Reson Med*. 2021;85(5):2377-2390. doi:10.1002/mrm.28627
6. Parker KJ, Szabo T, Holm S. Towards a consensus on rheological models for elastography in soft tissues. *Phys Med Biol*. 2019;64(21):215012. doi:10.1088/1361-6560/ab453d
7. Holm S. Spring–damper equivalents of the fractional, poroelastic, and poroviscoelastic models for elastography. *NMR Biomed*. 2018;31(10):e3854. doi:10.1002/nbm.3854
8. Islam MT, Righetti R. A new Poroelastography method to assess the solid stress distribution in cancers. *IEEE Access*. 2019;7:103404-103415. doi:10.1109/ACCESS.2019.2929021
9. Sowinski DR, McGarry MDJ, Van Houten EEW, Gordon-Wylie S, Weaver JB, Paulsen KD. Poroelasticity as a model of soft tissue structure: hydraulic permeability reconstruction for magnetic resonance elastography in silico. *Front Phys Ther*. 2021;8:8. doi:10.3389/fphy.2020.617582
10. Aichele J, Catheline S. Fluids Alter elasticity measurements: porous wave propagation accounts for shear wave dispersion in elastography. *Frontiers in Phys Ther*. 2021;9:9. doi:10.3389/fphy.2021.697990
11. Doyley MM. Model-based elastography: a survey of approaches to the inverse elasticity problem. *Phys Med Biol*. 2012;57(3):R35-R73. doi:10.1088/0031-9155/57/3/r35
12. Fovargue D, Nordsletten D, Sinkus R. Stiffness reconstruction methods for MR elastography. *NMR Biomed* 2018;31(10):e3935. doi:10.1002/nbm.3935
13. Aquino W, Bonnet M. Analysis of the error in constitutive equation approach for time-harmonic elasticity imaging. *SIAM J Appl Math*. 2019;79(3):822-849. doi:10.1137/18M1231237
14. Manuel I, Diaz MB. A modified error in constitutive equation approach for frequency-domain viscoelasticity imaging using interior data. *Comput Methods Appl Mech Eng*. 2015;296:129-149. doi:10.1016/j.cma.2015.07.025
15. Barbone PE, Gokhale NH. Elastic modulus imaging: on the uniqueness and nonuniqueness of the elastography inverse problem in two dimensions. *Inverse Probl*. 2004;20(1):283-296. doi:10.1088/0266-5611/20/1/017
16. McGarry M, Houten EV, Solamen L, Gordon-Wylie S, Weaver J, Paulsen K. Uniqueness of poroelastic and viscoelastic nonlinear inversion MR elastography at low frequencies. *Phys Med Biol*. 2019;64(7):75006. doi:10.1088/1361-6560/ab0a7d
17. Fernández-Cara E, Maestre F. An inverse problem in elastography involving Lamé systems. *J Inverse and Ill-Posed Probl*. 2018;26(5):589-605. doi:10.1515/jiip-2017-0065

18. Rouze NC, Wang MH, Palmeri ML, Nightingale KR. Parameters affecting the resolution and accuracy of 2-D quantitative shear wave images. *IEEE Trans Ultrason Ferroelectr Freq Control*. 2012;59(8):1729-1740. doi:10.1109/TUFFC.2012.2377
19. Wall DJN, Olsson P, Van Houten EEW. On an inverse problem from magnetic resonance elastic imaging. *SIAM J Appl Math*. 2011; 71(5):1578-1605. doi:10.1137/110832082
20. Van Houten EEW. Parameter identification in a generalized time-harmonic Rayleigh damping model for elastography. *PLOS One*. 2014; 9(4):1-9. doi:10.1371/journal.pone.0093080
21. Van Houten E, Paulsen K, Miga M, Kennedy F, Weaver J. An overlapping subzone technique for MR-based elastic property reconstruction. *Magn Reson Med*. 1999;42(4):779-786. doi:10.1002/(SICI)1522-2594(199910)42:4<779::AID-MRM21>3.0.CO;2-Z
22. Hannum AJ, McIlvain G, Sowinski D, McGarry MDJ, Johnson CL. Correlated noise in brain magnetic resonance elastography. *Magn Reson Med*. 2022;87(3):1313-1328. doi:10.1002/mrm.29050
23. Meyer T, Marticorena Garcia S, Tzschätzsch H, et al. Comparison of inversion methods in MR elastography: an openaccess pipeline for processing multifrequency shear-wave data and demonstration in a phantom, human kidneys, and brain. *Magn Reson Med*. 2022;88: 1840-1850. doi:10.1002/mrm.29320
24. Fovargue D, Kozerke S, Sinkus R, Nordsletten D. Robust MR elastography stiffness quantification using a localized divergence free finite element reconstruction. *Med Image Anal*. 2018;44:126-142. doi:10.1016/j.media.2017.12.005
25. Mei Y, Avril S. On improving the accuracy of nonhomogeneous shear modulus identification in incompressible elasticity using the virtual fields method. *Int J Solids Struct*. 2019;178-179:136-144. doi:10.1016/j.ijsolstr.2019.06.025
26. Warner J, Diaz M, Aquino W, Bonnet M. Inverse material identification in coupled acoustic-structure interaction using a modified error in constitutive equation functional. *Comput Mech*. 2014;54(3):645-659. doi:10.1007/s00466-014-1018-0
27. Diaz M, Aquino W, Bonnet M. A modified error in constitutive equation approach for frequency-domain viscoelasticity imaging using interior data. *Comput Methods Appl Mech Eng*. 2015;296:129-149. doi:10.1016/j.cma.2015.07.025
28. Grédiac M, Pierron F. Applying the virtual fields method to the identification of elasto-plastic constitutive parameters. *Int J Plast*. 2006; 22(4):602-627. doi:10.1016/j.ijplas.2005.04.007
29. Wang Y. Generalized viscoelastic wave equation. *Geophys J Int*. 2015;204(2):1216-1221. doi:10.1093/gji/ggv514
30. Hiscox LV, McGarry MDJ, Schwarb H, et al. Standard-space atlas of the viscoelastic properties of the human brain. *Hum Brain Mapp*. 2020;41(18):5282-5300. doi:10.1002/hbm.25192

How to cite this article: Van Houten E, Geymonat G, Krasucki F, Wattrisse B. General guidelines for the performance of viscoelastic property identification in elastography: A Monte-Carlo analysis from a closed-form solution. *Int J Numer Meth Biomed Engng*. 2023;39(8):e3741. doi:10.1002/cnm.3741